Thesis for the Degree of Master

A Study of the Process $e^+e^- \to c\bar{c}c\bar{c}$

by

Jaehyeok Yoo

Department of Physics

Graduate School

Korea University

January, 2009

Abstract

We describe the cross section measurement of $e^+e^- \to c\bar{c}c\bar{c}$ process at $\sqrt{s} = 10.52\,\mathrm{GeV}$. This study is based on 68 fb^{-1} data collected at KEKB with Belle detector. Experimentally, $e^+e^- \to D^0D^0 + X$ is measured with $D^0 \to K^-\pi^+$ decay mode. Monte Carlo generation is implemented by CompHEP and PYTHIA is used for the hadronization process. We report the cross section upper limit of $e^+e^- \to c\bar{c}c\bar{c}$ is $\sigma_{\text{upper limit at CL = 95 \%}}(e^+e^- \to c\bar{c}c\bar{c}) = 24.5\,\mathrm{pb}$ including systematic errors.

Acknowledgments

With a unlimited patience Prof. Eunil Won has guided me as an advisor. He has put students first and respected their wills so that they can do what they want in research. His keen insight and diverse experiences in research have challenged me. I am grateful for the opportunity to learn from him. I give my best thanks to him.

I thank Dr. Byeong Rok Ko. Without him this research may have not continued. His valuable advices and comments were given whenever my research needed ones. Dr. Boyoung Han also has thought with me about problems I faced and provided me with solutions. I am indebted to him.

I have enjoyed my lab life with other graduate students. Hyuncheong Ha has been my mental prop. His kindness and generosity has been a valuable asset of our lab. Soohyung Lee together with Hyuncheong Ha were my computer advisors. I owe much to them. My best American friend, Eugene Hong made an infinite contribution to my graduation. I always learn from him. I am also grateful to Guntae Park for making lab atmophere more friendly.

I would like to express my deepest thanks and love to my family for their constant love and support: father, mother, and sister. Without them I life may not be possible. Lastly, I give my thanks to the bride of May. She often reminded me of my vision when I was ignoring it. I also thank her for sculpting my rough personality. With her I could be a better person.

Soli Deo Gloria.

Contents

List of Figures

List of Tables

Chapter 1

Introduction

In nature forces are categorized into 4 kinds, gravitational, electromagnetic, weak and strong forces. All forces but gravity are described by Standard Model. The Standard Model explains what are the basic constituents of matter and how they interact with each other.

1.1 Standard Model

In Standard Model(SM), nature is composed of quarks, leptons and force carriers. Figure 1.1 shows the constituents of matter and force carriers responsible for the three interactions. The quarks and lepton are fermions because of their 1/2 spins and force carriers, photo, Z^0, $W^{\pm}$ and gluon are boson because of 1 spin.

Quarks are constituents of hadrons. For example, a proton is composed of two up-quarks and one down-quark. There are three pairs of quarks, up-down, charm-strange and top-bottom. They are also called three generations. The only difference between the generations is particle mass. For example, a top quark is 35000 times heavier than a up quark. This looks somewhat like a puzzle, but that is the way our nature is understood in SM . Table 1.2 shows quantum numbers of quarks, Q (charge), U (upness), (D) downness, (S) strangeness, (C) charmness, (B) bottomness, and (T) topness. There are 6-anti quarks with opposite charge. In addition to the above quantum numbers, quarks have color charges, R(red), G(green) and B(blue). Thus there are 36 quarks in total.

There are other kind of particles, leptons. Similar to quarks, they can be paired up into 3 generation. The three generations are electron-electron neutrino, muon-muon neutrino and tau-tau neutrino. The three generations and their corresponding

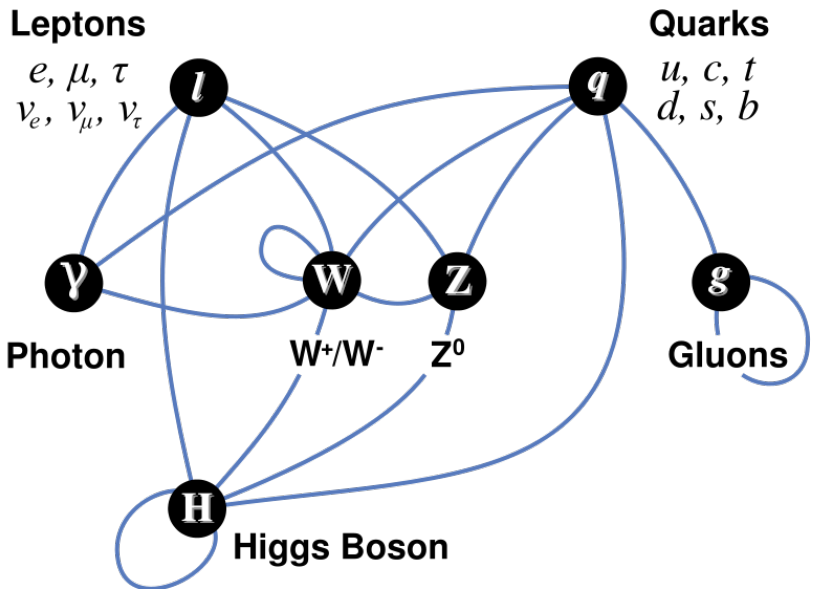

Figure 1.1: An illustration of particles and their interactions. Particles connected by lines have interactions with each other.

Table 1.1: Classification of quarks. q, Q, U, D, C, S, T, and B are quark, charge, upness, downness, charmness, strangeness, topness, and bottomness.

q	Q	U	D	C	S	T	B
u	2/3	1	0	0	0	0	0
d	-1/3	0	-1	0	0	0	0
c	2/3	0	0	1	0	0	0
s	-1/3	0	0	0	-1	0	0
t	2/3	0	0	0	0	1	0
b	-1/3	0	0	0	0	0	-1

Table 1.2: Classification of leptons. l, Q, L_e, L_μ, and L_τ are lepton, charge, electron number, muon number, and tau number.

l	Q	L_e	L_μ	L_τ
e	-1	1	0	0
ν_e	0	1	0	0
μ	-1	0	1	0
ν_μ	0	0	1	0
τ	-1	0	0	1
ν_τ	0	0	0	1

quantum numbers, Q (charge), L_e (electron number), L_μ (muon number), and L_τ (tau number). For each lepton, there are corresponding anti-leptons. Therefore, there are 12 leptons in total.

In SM interactions are described by exchanging force carriers and each interaction has its carriers. Photon is responsible for electromagnetic interaction, $W^\pm$ and Z for weak interaction and gluon for strong interaction. Gluons carry color charges, thus they can be distinguished by their color charges. There are 8 distinctive gluons. The Glashow-Weinberg-Salam theory requires at least one Higgs particle. Thus we have 12 leptons, 36 quarks, 12 force carriers and at least one Higgs particles. Therefore we have at the minimum 61 elementary particles in Standard Model.

1.2 Quantum Chromodynamics

The strong interaction is explained by QCD(Quantum Chromodynamics). This interaction is responsible for the binding of hadrons and hadron-hadron interactions. The interaction of photons with charged particles is described by Quantum Electrodynamics (QED). In QED, the coupling which is vertex factor in Feynman diagrams is $\sim 1/137$. Thus, diagrams with many vertices have little contributions to calculations. This means that perturbation theory is a proper tool for calculations. However, in QCD coupling is in the order of 1 and diagrams with many vertices are as important as ones with a few vertices. This situation makes the perturbation the-

ory no longer applicable. Another important feature of QCD is interaction of gluon. Photons interact with only charged particles. This means photon-photon interaction does not occur. However gluons carry color charges, thus gluon-gluon interaction does take place. This produces complicated situations. Nonetheless, some important features of QCD have been understood both theoretically and experimentally. They are confinement and asymptotic freedom.

Theorists can not manage the interactions between gluons in a long range because it is very complicated problem. In theory it seems impossible for gluon to have long range field while a massless particle, photon, same as gluon has long range fields. To remove this long range field problem, it is assumed that all physically existing particles have neutral color charge. This means there is no long range gluon fields because gluon fields of each quarks are cancelled out each other at long distance. All bound states of quarks have white color charge. This results in the fact that a single quark can not be separated from bound state. If one is detached, neither of them are color neutral. Thus such action is forbidden. This is confinement; the quarks are confined in a small region near one another. Hadronization that quarks and gluons form into hadrons is the result of this physical phenomenon. When two quarks become separated from some point it is energetically favorable for a new quark and anti-quark pair to appear simultaneously out of vacuum, than to allow the two quarks fly further. This is why quarks and gluons can not be observed experimentally. There are several models of hadronization. In PYTHIA [1], Lund model [2] is used.

As mention before, perturbation theory can not be used because of the large coupling contant. By the way, the coupling depends on energy not being contant. The higher energy becomes, the smaller the coupling gets. This is called asymptotic freedom. Thus in interactions that occur at high energy, perturbative expansion works as QED.

1.3 $e^+e^- \to c\bar{c}c\bar{c}$

The Belle collaboration has measured the cross section for the exclusive $J/\psi\eta_c$ production in e^+e^- annihilation at $\sqrt{s}$=10.6 GeV [3]:

$$\sigma[e^+e^- \to J/\psi\eta_c(\gamma)] \times \mathcal{B}(\eta_c \to \geqq 4 \text{ charged}) = 0.033^{+0.007}_{-0.006} \pm 0.009\,\text{pb}, \qquad (1.1)$$

while theory calculation claimed that

$$\sigma[e^+e^- \to J/\psi\eta_c] = 3.78 \pm 1.26\,\text{fb}\ [4], \tag{1.2}$$

$$\sigma[e^+e^- \to J/\psi\eta_c] = 5.5\,\text{fb}\ [5]. \tag{1.3}$$

The measured cross section was by an order of magnitude larger than what was expected from the calculation. A suggestion from theorists was made to look for an inclusive production of the four charmed particles [6] for e^+e^- collisions. One of

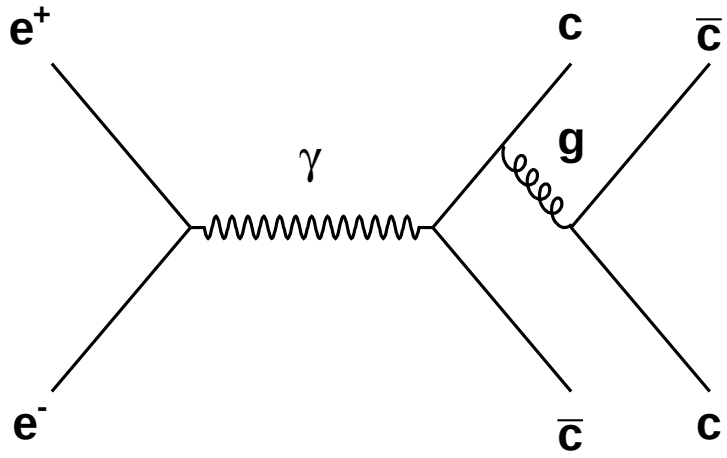

Figure 1.2: One of the Feynman diagrams for $e^+e^- \to c\bar{c}c\bar{c}$ at leading order in α and α_s.

the Feynman diagrams of the process $e^+e^- \to c\bar{c}c\bar{c}$ is illustrated in Figure 1.2. The authors of Ref. [6] predicted the cross section as

$$\sigma(e^+e^- \to c\bar{c}c\bar{c}) = 250\,\text{fb} \tag{1.4}$$

with charm quark mass 1.25 GeV. If a measurement is compatible with this value then calculation of hadronization part may have some flaws or new production mechanism exists. On the other hand, if much larger inclusive four charm cross section is measured as $e^+e^- \to J/\psi\eta_c$ cross section, we would cast doubts to the perturbative QCD calculation and perturbative expansion is not applicable for the prediction. This study was motivated from this question.

Meanwhile, recently the theorists came up with a solution and its calculation for the double charmonia cross section is [7]

$$\sigma[e^+e^- \to J/\psi\eta_c] = 17.6^{+8.1}_{-6.7}\,\text{fb} \tag{1.5}$$

which is in the same order as recently measured cross sections [8], [9].

Chapter 2

Belle Experiment

The data used in this analysis is taken by Belle detector at *High Energy Accelerator Research Organization (KEK)*. Originally, the aim of the Belle experiment is to observe CP violation effects in B meson decays and test the KM model predictions for CP violation. However, not only the B meson physics but also other interesting physics such as charm and tau physics are being studied. In this chapter, we describe the KEK B-Factory (KEKB) [10] electron-positron accelerator and the Belle detector.

2.1 The KEKB Accelerator

The KEKB accelerator is a high luminosity e^+e^- collider. The layout of the KEKB is illustrated in Figure 2.1. Its specification is listed on the Table 2.1. The

Table 2.1: Specification of KEKB accelerator.

Ring circumference	3 km
RF frequency	508 MHz
Electron energy	8 GeV
Positron energy	3.5 GeV
Design luminosity	$10^{34}\,\mathrm{cm}^{-2}\mathrm{s}^{-1}$
	more than 10^8 B meson($\Upsilon(4S)$) pairs/year

electrons are generated by an electron gun and accelerated in a LINAC (LINear

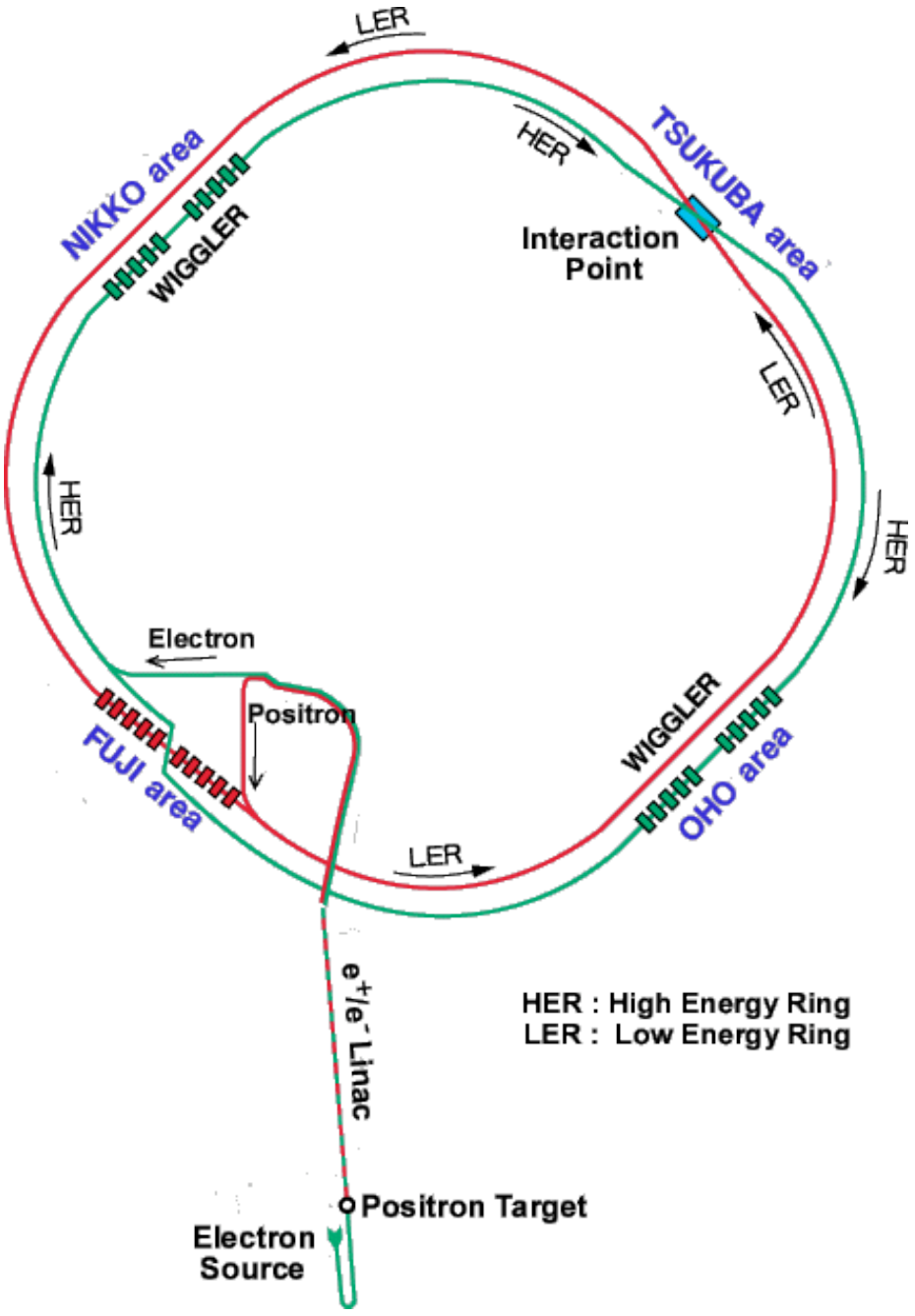

Figure 2.1: Schematic view of the KEKB storage ring.

ACcelerator). Once the electron energy reaches to 8.0 GeV, the electrons are shot into the HER (High Energy Ring). The pairs of electron and positron are produced by injected electron beam to a tungsten target. Positrons are shot into the LER (Low Energy Ring) after being separated and increasing energy up to 3.5 GeV in the LINAC. The electrons and positrons collide at one interaction point in Tsukuba area where the Belle detector in installed.

2.2 Belle Detector

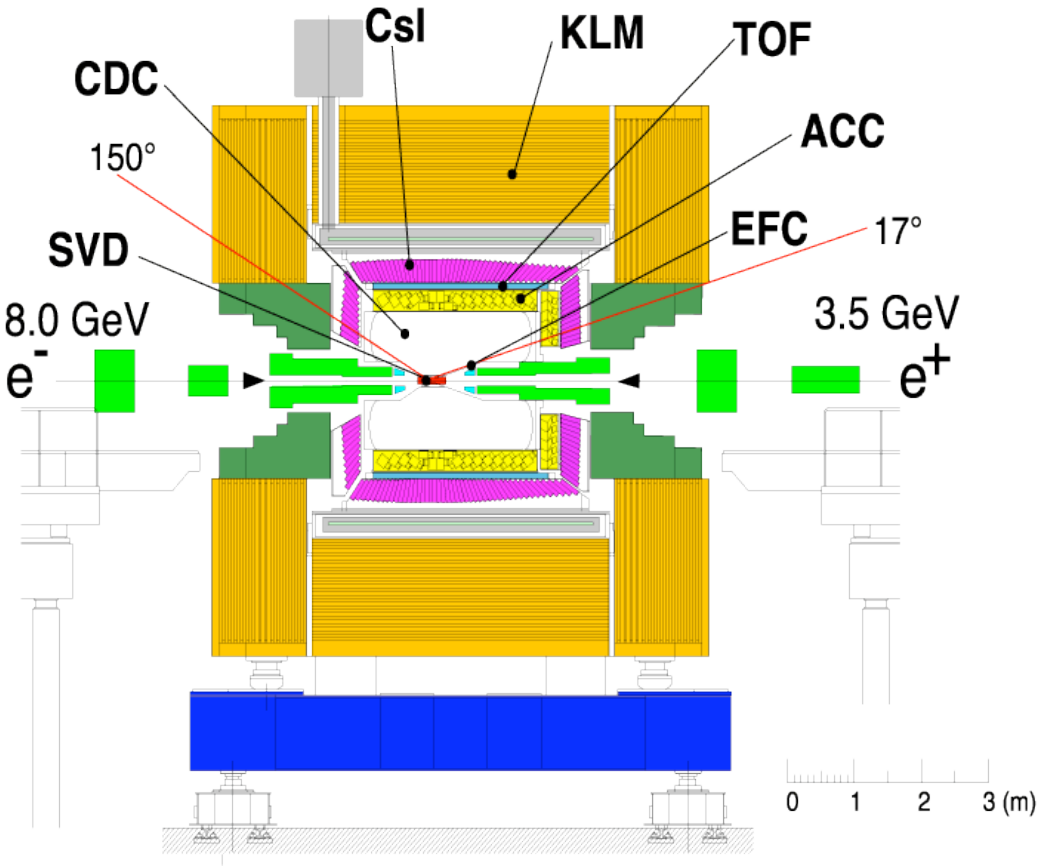

Figure 2.2: The side view of Belle detector.

The Belle detector [11] is composed of several sub-detectors. The side cross section view is shown in Figure 2.2 with each sub-detector and beam direction indicated.

2.2.1 Silicon Vertex Detector

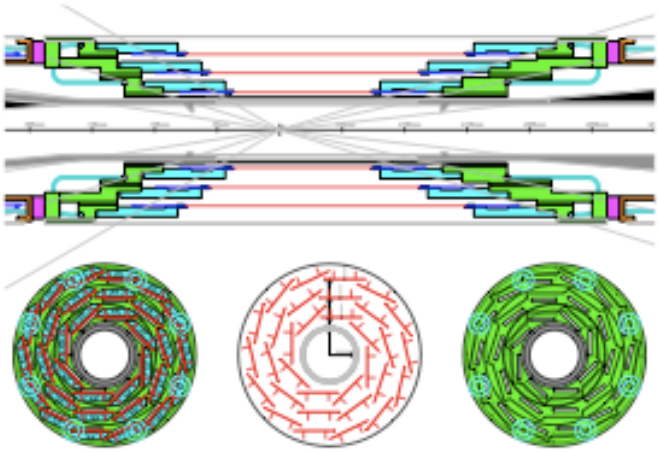

Figure 2.3: Configuration of SVD1. Top figure shows an r-z view and bottom figures show r-ϕ views.

In the innermost region to the beam pipe Silicon Vertex Detector (SVD) [12] is located to measure B meson decay vertices. The first version of SVD, SVD1, is composed of three layers of double-sided strip detectors (DSSD) and covers the region $23\,^\circ < \theta < 139\,^\circ$, 86 % of the solid angle. The three layers consist of 8, 10, and 14 ladders in the inner, middle, and outer layers, respectively (Figure 2.3).

Although basic performance of SVD1 was satisfactory, it had some limitations such as weak radiation tolerance, limited angular acceptance, relatively large radius of the innermost layer, and failure of the integrated AC coupling capacitor [13]. So, a new vertex detector, SVD2, was installed in 2003. It has four layers of DSSD and covers the region $17\,^\circ < \theta < 150\,^\circ$ which is nominal Belle angular coverage. The four layers are composed of 6, 12, 18, and 18 ladders in the first, second, third, and fourth layers respectively.

2.2.2 Central Drift Chamber

Outside of SVD, Central Drift Chamber (CDC) [14] performs the measurements of three-dimensional trajectory and momenta of charged particles. It also offers important information to the trigger system and particle identification information

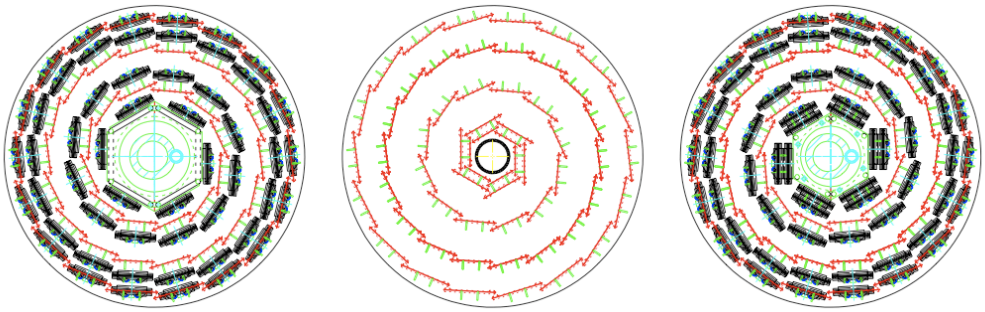

Figure 2.4: An r-ϕ view of SVD2. Compared with SVD1, the new design has one more layer and smaller radius of the innermost layer.

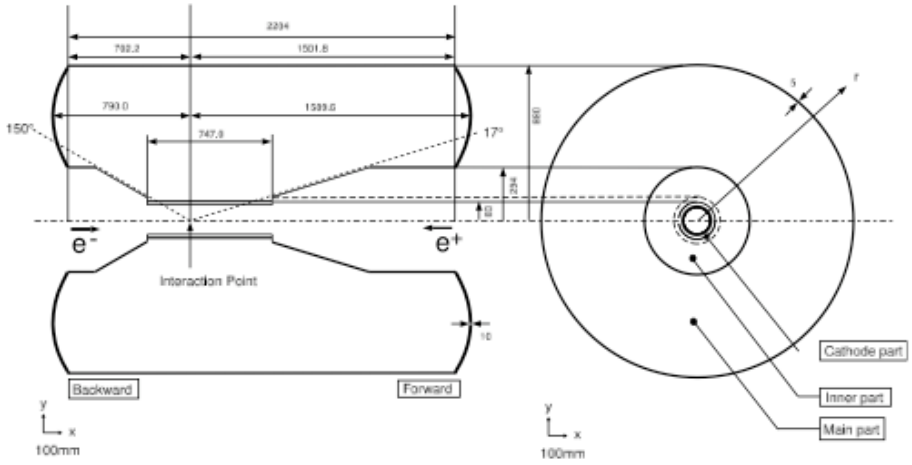

Figure 2.5: Schematic view of CDC structure. Left figure shows an r-z view and bottom figure shows r-ϕ views.

by precise dE/dx measurement. The structure of CDC is shown in Figure 2.5. The CDC covers region $17\,^\circ < \theta < 150\,^\circ$ and $r = 8.5 \sim 90\,\text{cm}$. The small r region has conical shape in order to prevent accelerator components and maximize acceptance. The chamber has small square cell structure and 50 cylindrical layers. 11 super layers are organized between four layers to attain highly efficient and fast z-trigger. 50:50 mixture of Helium and Ethane is used to reduce multiple scattering. When particle a particle pass a gas chamber, it loose it energy by gases are ionized by acquiring energy from the incident particle. The ionized particles drift to the sense wires to which high voltage (2.4 kV) is applied. A simple schematic view of this process is illustrated in Figure 2.6.

2.2.3 Aerogel Cherenkov Counter

When a charged particle moves faster in a medium than the speed of light in the medium, Cherenkov radiation happens. The speed of light in a medium of refraction index, n, is

$$v = c/n \tag{2.1}$$

where c is the speed of light in vacuum. In order for Cherenkov radiation to occur, the speed of particle must be faster than this. In such condition, an electromagnetic shock wave is created. ACC [15] detects this light. Pions can produce Cherenkov radiation in ACC whose refractive index is from 1.01 to 1.03. while aerogel is insensitive to charged kaons below 3.5 GeV. Thus ACC is designed to distinguish charged pions and kaons in momentum range $1.5\,\text{GeV} \sim 3.5\,\text{GeV}$. There are 5 aerogel tiles in an ACC module whose size is $12\,\text{cm} \times 12\,\text{cm} \times 12\,\text{cm}$. 960 counter modules are installed in barrel region and 228 modules at forward endcap part of the detector. The Cherenkov light is detected by fine-mesh photomultipliers (FM-PMT) which is designed to operate in a strong magnetic fields. It is operated in 1.5 T magnetic field.

2.2.4 Time Of Flight

Time Of Flight (TOF) [16] detector is used to distinguish K from π for momentum below $1.2\,\text{GeV/c}$ [17]. It also offers precise event timing to Belle trigger system. The TOF and TSC configuration is shown in Figure 2.7. One TOF module consists of two TOF counters and one Trigger Scintillation Counter (TSC). TOF counters

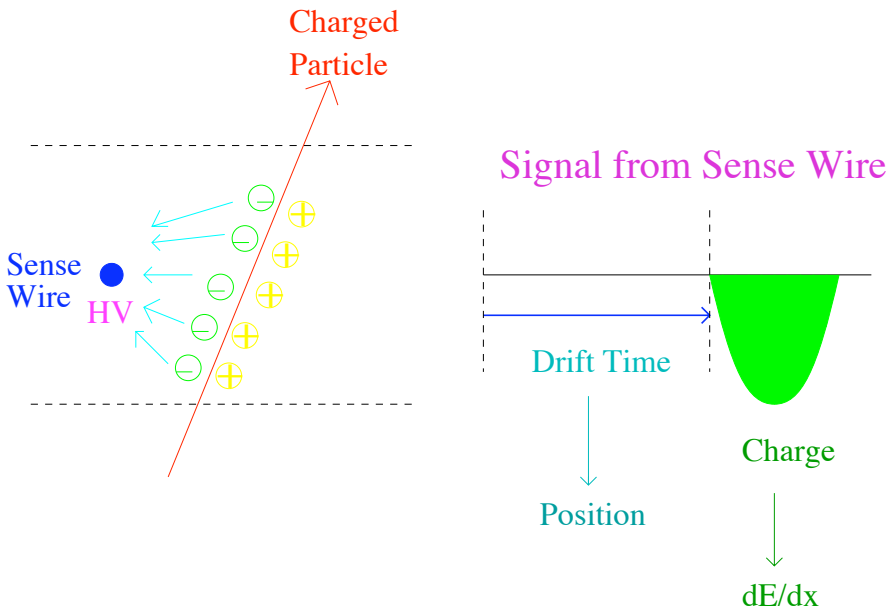

Figure 2.6: Schematic view of the process when a charged particle passes through CDC. When a charged particle passes through CDC, the gases are ionized and drift to the high voltage sense wires.

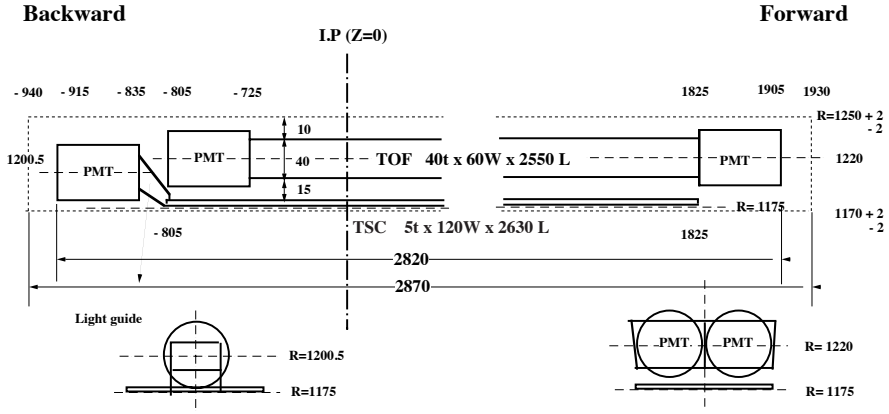

Figure 2.7: Configuration of TOF and TSC. Two TOF counters and one TSC form a one TOF module.

Table 2.2: Specification of TSC and TOF.

cntr	scinti	z cm	inner radius	thick cm	seg.
TSC	BC412	-80.5∼182.5	118.0	0.5	64
	air-gap			1.5	
TOF	BC408	-72.5∼182.5	120.0	4.0	128

are at both ends while TSC is only at backward end. There are 128 TOF counters and 68 TSC at radius 120 cm (Table 2.2). It covers region $33\,^\circ < \theta < 121\,^\circ$. A charged particle whose transverse momentum is less than 0.28 GeV/c can not reach TOF.

2.2.5 Electromagnetic Calorimeter

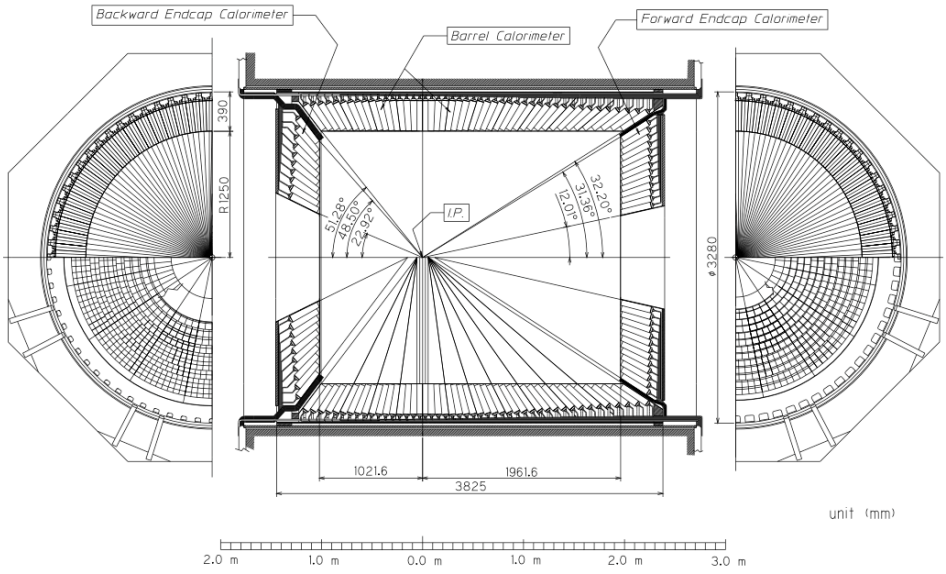

Figure 2.8: Configuration of ECL.

Electromagnetic Calorimeter (ECL) [18] detects the photons from B meson decays with high efficiency and good resolution. Most of them are products of decay cascade, they have relatively low energy. Thus good performance below 500 MeV is of great import. ECL is also used for electron identification by comparison of the charged particle track momentum and the energy is deposits in ECL. Fine-grained segmentation of calorimeter is required because high momentum π^0 detection needs high resolution of two close photons and precise determination of their opening angle. The whole calorimeter has 3.0 m long and 1.25 m inner radius section and endcap sections at z = 2.0 m and -1.0 m. The overall configuration of ECL is shown in Figure 2.8.

Table 2.3: The geometrical parameters of the CsI calorimeter.

	θ coverage	θ seg.	ϕ seg.	# of crystals
Forward Endcap	11.7 ° - 31.5 °	13	48 - 128	1168
Barrel	32.2 ° - 128.7 °	46	144	6624
Backward Endcap	130.8 ° - 158.3 °	10	64 - 144	1024

ECL is composed of array of CsI(Tl) crystal and geometrical parameters are given in Table 2.3. Each crystal is tower-like and faces almost interaction point. The entire calorimeter covers 91 % of solid angle; $17.0\,^\circ < \theta < 150\,^\circ$. An independent pair of silicon PIN photodiodes and charge sensitive preamplifiers are attached at the end of the each CsI(Tl). The preamplifier output is sent to a shaping circuit for the two signals from the same crystal are to be summed. The summed signal is split for main ADC and trigger electronics.

Chapter 3

Analysis Tools and Techniques

Monte Carlo simulation is done by CompHEP, Belle-EvtGen, and Geant based computer simulator. The modified Super Fox Wolfram moment reduces backgrounds significantly and the signal yields are extracted by sideband subtraction. Finally the cross section upper limit is calculated based on the idea of Bayes' Theorem.

3.1 Monte Carlo Simulation

Figure 3.1 shows overall Monte Carlo simulation flow. Event generation was done by CompHEP [19], hadronization and decay by Belle-EvtGen [20], and detector simulation was implemented by Geant [21] based computer simulation (GSIM [22]).

3.1.1 $e^+e^- \to c\bar{c}c\bar{c}$ generation by CompHEP

The $e^+e^- \to c\bar{c}c\bar{c}$ process may not simply be generated by usual Belle-EvtGen since it is not a typical 2-2 process in the tree level. PYTHIA [1] which is embedded in EvtGen does not have full matrix elements for 2-4 process. We have looked into this issue and found an alternative method. It is CompHEP [23] which is able to produce 2-4 processes in tree level. CompHEP generates $e^+e^- \to c\bar{c}c\bar{c}$ process leaving 3 momenta of the 4 charm and anti-quarks as an output. Once the four quark momenta were obtained, we put the output into the Belle-EvtGen. A careful study was done in order to interface CompHEP and the PYTHIA within the Belle software framework.

The validity of CompHEP generation was confirmed by comparing with a full 2-4 matrix element calculations [6]. In Figure 3.2, (a) the differential cross sections of

Figure 3.1: Monte Carlo simulation flow. CompHEP generates $e^+e^- \rightarrow c\bar{c}c\bar{c}$ events and Belle-EvtGen is responsible for hadronization and particle decays. Detector simulation is done by Geant based computer simulator (GSIM).

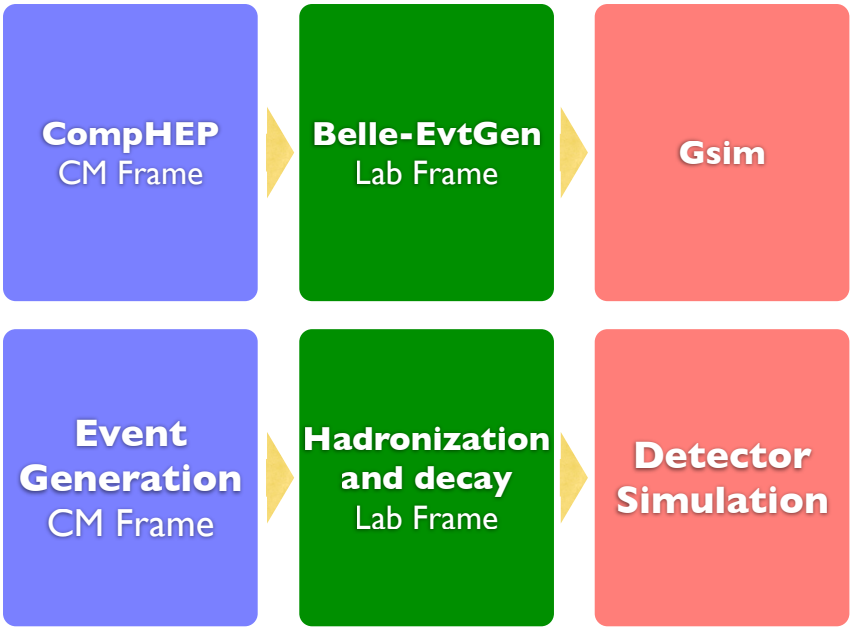

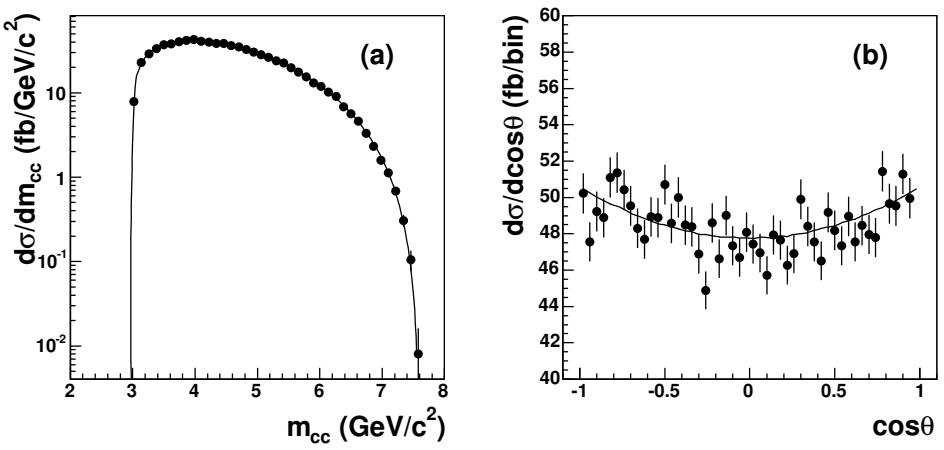

Figure 3.2: Differential cross sections of (a) $d\sigma/dm_{cc}$ as a function of m_{cc} in fb/(0.12 GeV) with respect to the invariant mass m_{cc} and (b) $d\sigma/dm_{\cos\theta}$ in fb/(0.04) with respect to the angle between the cc system and the direction of the incoming electron. Points with error bars show the results from the CompHEP, and the curves represent results from analytic calculations [6]. 100K events were generated.

$d\sigma/dm_{cc}$ with respect to the invariant mass m_{cc} and (b) $d\sigma/d\cos\theta$ with respect to the angle between the cc system and the direction of the incoming electron are shown. Both distributions show good agreement between the CompHEP generation and the analytic calculation, which indicates validity of CompHEP as a MC generator.

3.1.2 Hadronization and Decay by Belle-EvtGen

The success of implant of CompHEP output to Belle-EvtGen was confirmed in two ways, comparing 1) the number charm quarks generated and 2) the angular distribution of charm quark momentum in CM frame.

1) was done by counting all prompt charmed particles, charmonia, charmed mesons and charmed baryons. For 100K $e^+e^- \to c\bar{c}c\bar{c}$ events, we have 200K charm quarks and the counted number of charmed particles was 200K. We could see that the interface between CompHEP and Belle-EvtGen successfully worked and the charm quarks were properly fragmented. The rest decay processes totally depend on PYTHIA in Belle-EvtGen.

For 2), we compared the $\cos\theta$ distributions, where θ is an angle between the momentum and the beam axis, of charm quarks from CompHEP and D mesons from Belle-EvtGen. Similarity is expected since D mesons acquire their momenta

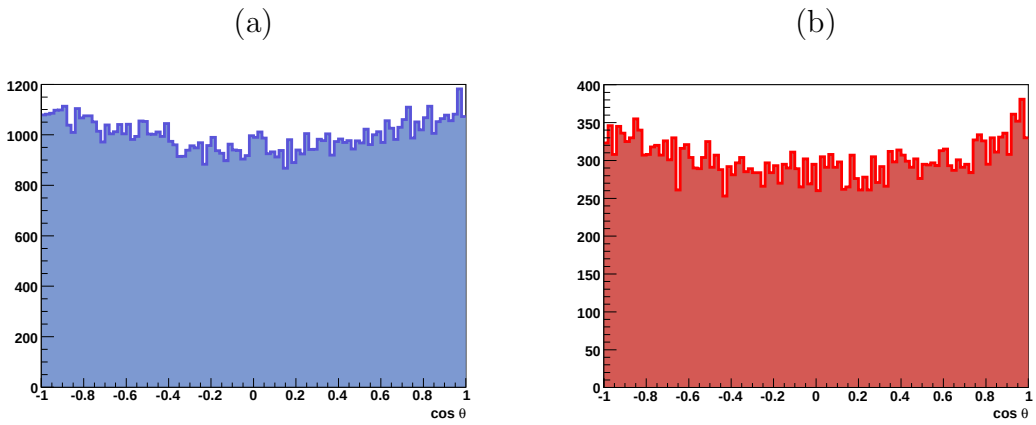

Figure 3.3: $\cos\theta$ of (a) charm quark momenta in CompHEP output and (b) D^+ momenta in generator level of Belle-EvtGen. θ is the angle between the momentum and the beam direction. Both are in the CMS frame.

primarily from charm quarks.

Table 3.1: Branching fraction (BF) of D^+/D^- and $D^0/\bar{D}^0$. BF(Belle-EvtGen) are obtained by dividing the total number of generated D mesons by the number of D mesons which decay into $K^\mp\pi^\pm\pi^\pm(D^+/D^-)$ and $K^\mp\pi^\pm(D^0/\bar{D}^0)$, respectively. BF(`DECAY.DEC`) is the branching fraction in `DECAY.DEC`. `PHOTOS PHSP` model is used in `DECAY.DEC`.

mode	BF(Belle-EvtGen)	BF(`DECAY.DEC`)
$D^+ \to K^-\pi^+\pi^+$	0.0524 ± 0.0004	0.0531
$D^- \to K^+\pi^-\pi^-$	0.0538 ± 0.0004	0.0531
$D^0 \to K^-\pi^+$	0.0384 ± 0.0002	0.0382
$\bar{D}^0 \to K^+\pi^0$	0.0380 ± 0.0002	0.0382

From Figures 3.3, we can see the similarity of both distributions. Branching fractions of D^+ and D^0 (and their charge conjugates) by counting in generation level are on Table 3.1 with the branching fractions in `DECAY.DEC` [20] of Belle-EvtGen. The Branching fractions on the table show consistency with each other. In both decays of D^+ and D^0 , `PHOTOS PHSP` [20] decay model was applied, rather than `D_DALITZ` [20] model for $K\pi\pi$. From the two comparisons, we conclude that the generation and embedment of CompHEP to Belle-EvtGen are successfully done. One thing to note is that the CompHEP generation is done in e^+e^- CM frame, while

the Belle-EvtGen in lab frame. For some reason, only does CM-lab combination give total generation in lab frame. This was confirmed by boosting D^+ to CM frame and comparing this with CM-CM combination which is obviously a total CM frame generation.

3.1.3 Detector Simulation

The validity was confirmed by comparing numbers of reconstructed D^+ candidates at generator level with the number of reconstructed D^+ after detector simulation. At both stages, D^+ was reconstructed by using $K^-\pi^+\pi^+$ mode. The number of total $e^+e^- \to c\bar{c}c\bar{c}$ events is 100K.

Table 3.2: Number of signal events (D^+D^+) at generator level and detector simulation. D^+ were reconstructed by $K^-\pi^+\pi^+$ mode. Signal tracking efficiency, $\epsilon_{\text{detector}}$, is multiplied to the counted number in generator level as many times as the number of charged tracks, 6. This number is compared with the number of D^+D^+ events after detector simulation.

	generator level	detector simulation
counted number	2390 ± 50	
detector efficiency $\epsilon_{\text{detector}} = 0.8 \pm 0.1$	$\mathbf{600 \pm 400}$	$\mathbf{540 \pm 20}$

The number 2390 was obtained by simply counting events with more than two D^+ candidates which are within the mass window $|M_{K^+\pi^-\pi^-} - M_{D^+}| < 0.012$ GeV. Supposing the detector efficiency of one charged track is 0.8 ± 0.1, we obtain 600 ± 400 events from the simple relation,

$$\epsilon_{\text{detector}} N_{\text{true}} = N_{\text{measure}}. \tag{3.1}$$

The number of signal events obtained from detector simulation is 540 ± 20, which is consistent with the one in generator level. We can conclude that detector simulation is done properly.

3.2 Modified Super Fox Wolfram moment

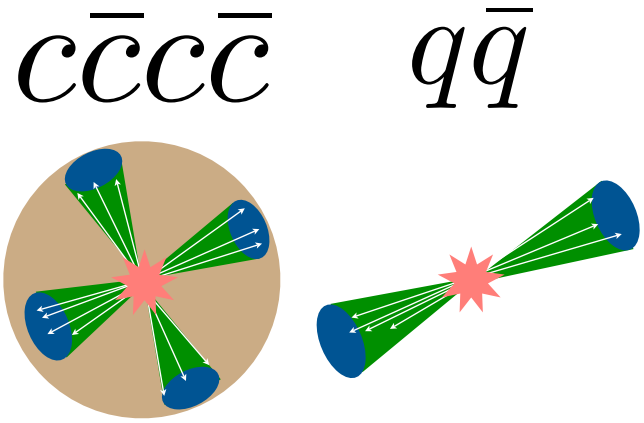

Figure 3.4: The event shapes of $c\bar{c}c\bar{c}$ and $q\bar{q}$ events. Since $c\bar{c}c\bar{c}$ events are four-jet-like, the overall event shape is likely to be spherical while $q\bar{q}$ events are two-jet-like.

The normal $q\bar{q}$ events such as $c\bar{c}, u\bar{u}, d\bar{d}$ and $s\bar{s}$ have two-jet-like event shapes. In CM frame of $q\bar{q}$, the quark and the anti-quark fly in the opposite direction because of momentum conservation. During their flight they are hadronized and subsequent hadrons obtain their momenta primarily from the quarks. The hadrons decay into other particles and the event look like two jets. However, the $c\bar{c}c\bar{c}$ events are four-jet-like and their event shapes are likely to be spherical. Fig 3.4 show the event shape difference graphically. It is this event shape discrepancy that one can distinguish four charm events from $q\bar{q}$ events.

We take advantage of the modified Super Fox Wolfram moment [24] which can be calculated by following steps.

1. Calculate 17 event shape variables,

```
Roo0  Roo1  Roo2  Roo3  Roo4
Rso00 Rso01 Rso02 Rso03 Rso04
Rso10 Rso12 Rso14
Rso20 Rso22 Rso24
Pt
```

where Rso and Roo are Hoo/Hmax and Hso/Hmax, respectively and Pt is transverse

momenta. The original Fox Wolfram (FW) moment [25] is defined by

$$H_l = \sum_{i,j} \frac{|\vec{p}_i||\vec{p}_j|}{s} P_l(cos\phi_{ij}) \tag{3.2}$$

where $P_l(cos\phi_{ij})$ is Legendre polynomials, i and j run over all hadrons in an event, and ϕ_{ij} is the angle between particles i and j. We can categorize H_l into three kinds, Hss, Hso, and Hoo. Hss is when i and j are all D^0. Hso is when i is D^0 but j is other particles. Finally, Hoo is when i and j are all other particles. Then we have relation H = Hss + Hso + Hoo. For KSFW moment only are Hso and Hoo used. Hso has two indices while the original FW has only one. The first index in Hso indicates types of the other particles, 0 for the charged, 1 for the neutral, and 2 for the missing particles. The distributions of the 17 variables for signal MC and sideband of real data are shown in Appendix A.

2. Construct a Fisher discriminant [26] by linear combination of the 17 variables. The Fisher discriminant is defined by

$$F = \sum_{i=1}^{17} \alpha_i x_i \tag{3.3}$$

where x_i are the 17 variables. α_i is determined by

$$\alpha_i = \sum_{j=1}^{17} (\Sigma_{sig} + \Sigma_{bkg})^{-1}_{ij} (\bar{x}_{sig} - \bar{x}_{bkg})_j \tag{3.4}$$

where Σ_{ij} is a correlation coefficient of x_i and x_j and $\bar{x}_j$ is mean of x_j. This condition gives the best separation between the signal and background distributions. The Fisher discriminants are classified to 7 categories according to their *missing* $mass^2(mm^2)$.

3. Using the obtained F at 2., construct probability distribution functions (pdf) in 7 mm^2 regions. In each region, signal and background distributions give corresponding likelihoods at the end.

4. Given KSFW distributions of signal and background, we do fitting with an asymmetric Gaussian function and obtain fit parameters. Signal and background likelihoods are calculated using the parameters and we use likelihood ratio, $klr = \mathcal{L}_s/\mathcal{L}_s + \mathcal{L}_b$, as a cut variable, where $\mathcal{L}_s$ and $\mathcal{L}_b$ are signal and background likelihood

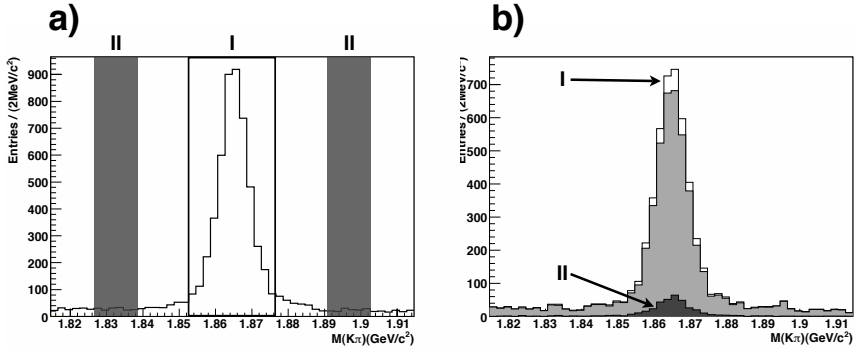

Figure 3.5: a) the invariant mass distribution of the first D^0 and b) second D^0. In a) signal region(I) and sideband region(II) are specified. I and II in b) indicated that the corresponding first D^0 is in I and II region in a). The light gray histogram in b) is the sideband subtracted histogram.

ratio, respectively. The KSFW pdfs of signal MC and sideband of real data are shown in Appendix A.

3.3 Sideband Subtraction

In order to extract the signal yield, the method of sideband subtraction is used. An advantage of this method is that we can cut off combinatorial backgrounds by fitting. Since there are two D^0s in a signal event, we reconstruct 2 D^0 candidates. Here we do not select the best candidates because the random combinations will be subtracted at the end. To the two candidates, we assign indices, first and second D^0. Table 3.3 shows all possible combinations of the two D^0s. We need to choose only combination A and it can be carried out by following steps.

1. Draw the invariant mass distribution of the 2nd D^0 when the first D^0 is in

Table 3.3: All combinations of the two D^0 candidates. D^0 means the real D^0 and X means combinatorial background. Real signal events correspond to combination A.

combination	first D^0	second D^0
A	$\mathbf{D^0}$	$\mathbf{D^0}$
B	D^0	X
C	X	D^0
D	X	X

the signal region. The region I in a) of Figure 3.5 shows the signal region of the first D^0 and I in b) shows the invariant mass distribution of the second D^0 for signal region first D^0. The I in b) includes all four combinations.

2. Draw invariant mass distribution of the 2nd D^0 when the first D^0 is in the sideband region. The region II in a) of Figure 3.5 shows the sideband region of the first D^0 and II in b) shows the invariant mass distribution of the second D^0 for sideband region first D^0. Since the first D^0 in the sideband region, this histogram contains combination C and D only.

3. Subtract the histogram II from I. The resultant light gray histogram in Figure 3.5 is the sideband subtracted histogram. Because combination C and D are subtracted, the subtracted histogram contains only A and B.

4. The last step is to do fitting to the subtracted histogram. The combinatorial backgrounds (combination B) have a shape of the first polynomial. Thus, with fit function, $signal\,function + fisrt\,polynomial$, only can signal be extracted.

To validate the result of sideband subtraction one can do 2 dimensional fitting to M(first D^0) vs. M(second D^0) distribution. The comparison is described in Appendix B.

3.4 Cross Section and Upper Limit

When no significant excess of signal is seen in measurements we set upper limit

at certain confidence level. In the Belle experiment the optimization of cut values are determined by *Figure Of Merit*, which is defined to be

$$F.O.M. = \frac{S}{\sqrt{S+B}} \tag{3.5}$$

where S and B are signal and background, respectively. However, for the measurements whose expected signal events are not known, using *Figure Of Merit* is meaningless. In this case, the upper limit is used to optimize cut value by maximizing sensitivity.

The total cross section is calculated by

$$\sigma(e^+e^- \to cc + X) = \frac{N_{\rm data} - N_{\rm bkg}}{\epsilon_{\rm sig} \times \mathcal{L}_{\rm int} \times BF(D^0 \to K^-\pi^+)^2 \times P(c \to D^0)^2} \tag{3.6}$$

where $N_{\rm data}$ is the number of events in data, $N_{\rm bkg}$ is the number of event estimated in background MC, $\epsilon_{\rm sig}$ is the efficiency of the given set of selection criteria for selecting $D^0D^0 + X$ events, $\mathcal{L}_{\rm int}$ is the integrated luminosity, BF is branching fraction and $P(c \to D^0)$ is the ratio of $c \to D^0$ to $c \to X$. We use $P(c \to D^0) = 0.565$ [27]. Supposing there is no signal, we can calculate the upper limit of cross section at certain confidence level. Even though $N_{\rm data}$ has to be Poisson-fluctuated, we can ignore it for simple calculation. In this case, we have

$$\sigma_{\text{upper limit}} = \frac{\delta N_{\rm bkg}}{\epsilon_{\rm sig} \times \mathcal{L}_{\rm int} \times BF(D^0 \to K^-\pi^+)^2 \times P(c \to D^0)^2} \tag{3.7}$$

and the numerator varies by confidence level. The $N_{\rm bkg}$ follows the Poisson distribution,

$$P(n|\mu, I) = \frac{e^{-\mu}\mu^n}{n!} \tag{3.8}$$

where I is all information used to construct μ. $P(n|\mu, I)$ is interpreted as 'for a given mean, μ, the probability of measuring n events'. We can put the $N_{\rm bkg}$ to μ and find n up to which integration of $P(n|\mu, I)$ gives 0.95. The thing is that since n is a positive integer, integration may not give exactly 0.95. However, because we are dealing with a conditional probability, we may solve this problem by Bayes' Theorem [28],

$$P(\mu|n, I) \propto \frac{e^{-\mu}\mu^n}{n!} P(\mu|I). \tag{3.9}$$

The RHS is normalized so that integration is 1 and a priori probability, $P(\mu|I)$ is assumed to be constant. Now we have different interpretation that 'for a given n, the probability of its mean being μ.'

There comes another problem in interpreting the $N_{\rm bkg}$ as n because $N_{\rm bkg}$ is rarely an integer. It is obtained by fitting and it rarely gives integers while n should be integers. So we Poisson-fluctuated $N_{\rm bkg}$ and obtained distribution of

$$\bar{\mu}_{\text{ at 95 \% with } n} = P(n|N_{bkg}, I) \times \mu_{\text{ at 95 \% with } n} \tag{3.10}$$

where $\mu_{\text{ at 95 \% with } n}$ is the μ at which C.L. is 95 % for given n. We use $\bar{\mu}_{\text{ at 95 \% with } n}$ for $\delta N_{\rm bkg}$ at C.L. = 95 %.

Chapter 4

Event Selection and Signal Extraction

In this analysis, we reconstruct $D^0/\bar{D}^0$ that decay into $K^{\mp}\pi^{\pm}$ final states. With candidates that pass several criteria listed below, we do sideband subtraction and fitting for the signal yield extraction. In addition, systematic errors are studied. Data was taken at $\sqrt{s} = 10.52$ GeV and $\mathcal{L}_{\rm int} = 68$ fb^{-1}.

4.1 Event Selection

The D^0 candidates selection criteria are as follows.

- $|dz| < 4.0\,\mathrm{cm}, |dr| < 2.0\,\mathrm{cm}$
- $\mathcal{L}_{K/\pi} > 0.55$ for K and $\mathcal{L}_{K/\pi} < 0.55$ for π
- $|M_{K^-\pi^+} - M_{D^0}| < 0.012\,\mathrm{GeV/c^2}$
- pass vertex fit
- number of $K^{\mp} > 1$ and number of $\pi^{\pm} > 1$ in one event
- klr > 0.85

The mass window is determined by signal Monte Carlo simulation. The invariant mass distribution of $M_{K^-\pi^+}$ with the signal mass window is shown in Figure 4.1. The klr distributions of a) sideband of real continuum data and b) signal MC is shown in Figure 4.2. The two distributions are clearly separated to 0 and 1. The klr

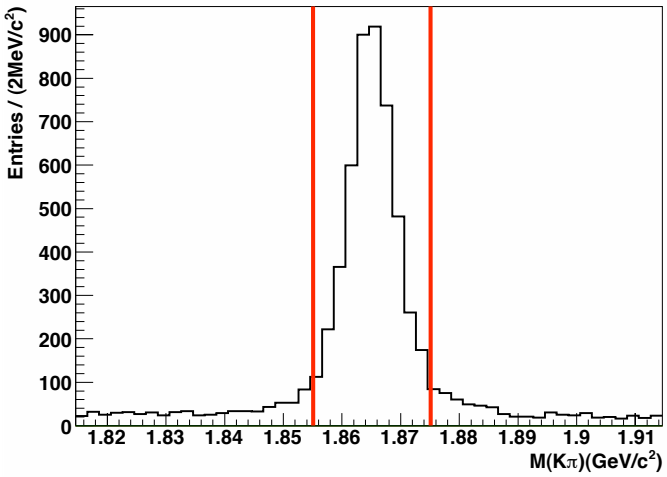

Figure 4.1: Invariant mass distribution $M_{K^-\pi^+}$ and signal region.

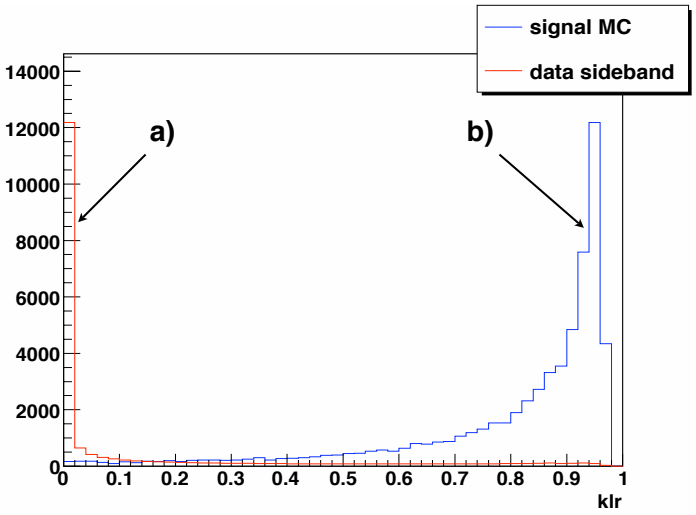

Figure 4.2: The klr distribution of a) sideband of real data b) signal MC.

is optimized by minimization of the cross section upper limit supposing no signal is observed. In order to obtain the yields in the signal window, we do fitting to the sideband subtracted invariant mass distribution of the second D^0. The real continuum data at $\sqrt{s} = 10.52$ GeV is used to remove systematic uncertainties due to background modeling. Total luminosity of the available continuum data is $68\,\mathrm{fb}^{-1}$.

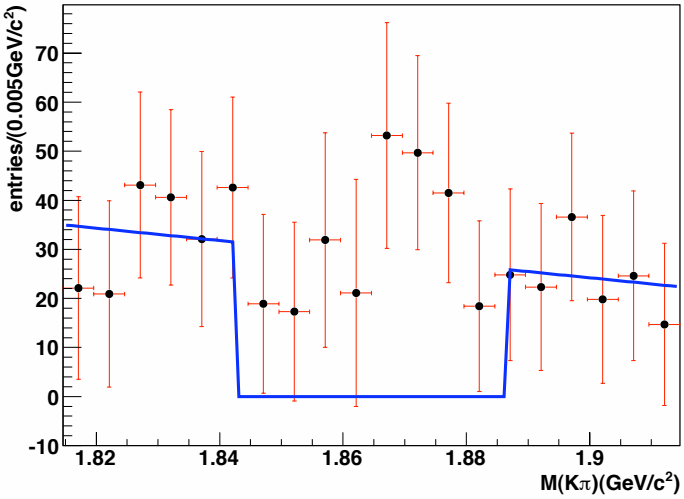

Figure 4.3: Sideband subtracted distribution of the second D^0. Fitting is done only to the sideband region to determine the background level in signal the region in case no signal is observed.

Figure 4.3 shows the fitting done only in the sideband region. The fit function is $first\,polynomial$. From the obtained fit function we calculate the yields in the signal region. By doing this and calculating the cross section upper limit with various klr, we optimize the klr value at which the upper limit is least. Figure 4.4 shows the cross section upper limit at C.L.=95 % with various klrs. The upper limit has its minimum , 5.2 pb, when $klr > 0.85$.

4.2 Signal Extraction

By using sideband subtraction method we can obtain the number of signal events. Figure 4.5 shows the invariant mass distributions of the second D^0 when the first D^0 is in a) signal region and b) sideband region. The c) is the subtracted second

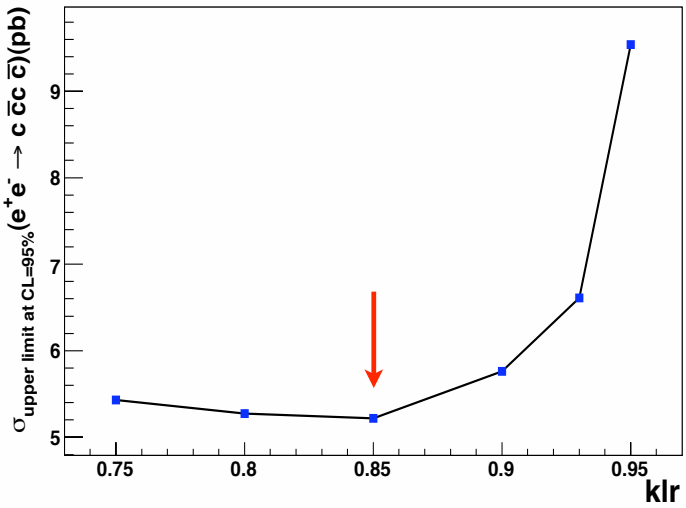

Figure 4.4: Cross section upper limit at C.L. = 95 % with respect to klr. At klr=0.85, the cross section upper limit is least and the corresponding cross section is 5.2 pb.

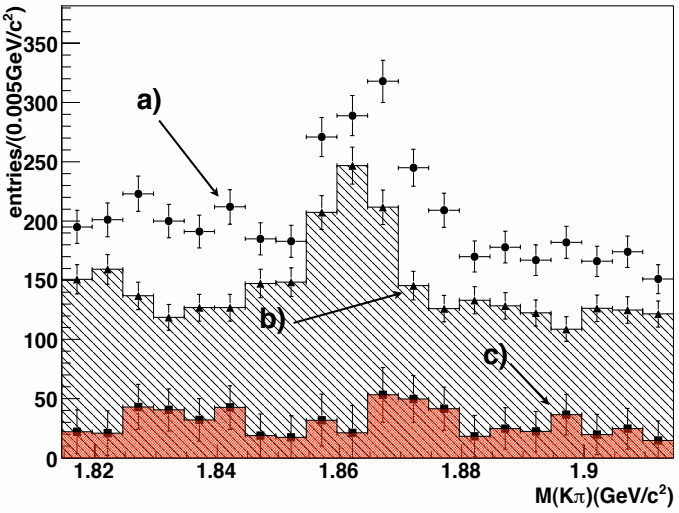

Figure 4.5: Invariant mass distribution of the second D^0. 68 fb^{-1} continuum data at $\sqrt{s}$ = 10.52 GeV is used. a) and b) are when the first D^0 is in signal region and sideband region, respectively. c) is the sideband subtracted second D^0 invariant mass distribution to which fitting is done. Only are statistical errors included.

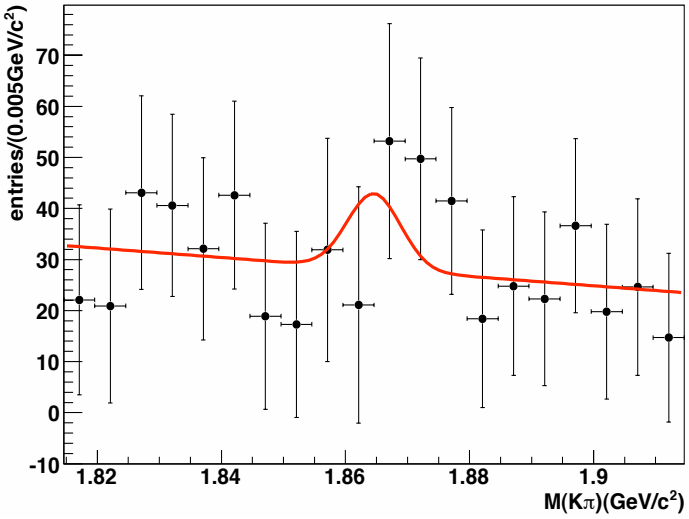

Figure 4.6: Fitting to the sideband subtracted histogram. Errors are statistical only.

D^0 mass distribution. A fitting with a function,

$$Gaussian + first\,polynomial. \tag{4.1}$$

is done to the sideband subtracted second D^0 mass distribution. The mean and width of the Gaussian are fixed to the nominal D^0 mass, 1.8646 GeV, and 0.0043 GeV/c^2, respectively. The width is obtained from signal Monte Carlo. The signal yield is counted by integrating the Gaussian in $\pm 3\sigma$ region and dividing the result by 0.1 GeV/20, mass window per bin.

4.3 Systematic uncertainties

Two sources of systematic uncertainties are listed on Table 4.1. All systematics are added in quadrature.

- charm quark mass variation

  In CompHEP generation the charm quark mass is varied from nominal mass, 1.25 GeV/c^2. The corresponding signal efficiencies at each mass are on the Table 4.2. The uncertainty to the signal efficiency is

  $$\Delta\epsilon_{\rm sig} = 0.007 \tag{4.2}$$

  and its contribution to the cross section is 9.1 %.

Table 4.1: Sources of systematic uncertainties and their contributions to the $e^+e^- \rightarrow c\bar{c}c\bar{c}$ cross section.

Source	Contribution (%)
charm quark mass variation	9.1
fit bias	19
Total	21 %

Table 4.2: Signal efficiencies at various charm quark masses in CompHEP generation.

charm quark mass ($\mathrm{GeV/c^2}$)	1.1	1.25	1.5	1.6
ϵ_{sig}	0.089	0.087	0.091	0.094

- fit bias

Table 4.3: Number of signal yields in various fit regions. The bin size is fixed to $0.005\,\mathrm{GeV/c^2}$.

fit region ($\mathrm{GeV/c^2}$)	1.8046 $\sim$ 1.9246	1.7946 $\sim$ 1.9346	1.7846 $\sim$ 1.9446	1.7746 $\sim$ 1.9546	1.7646 $\sim$ 1.9646
signal yields	34 ± 42	31 ± 42	29 ± 42	29 ± 42	27 ± 41

With a fixed bin size, $0.005\,\mathrm{GeV/c^2}$, the fit region is gradually increased from $0.1\,\mathrm{GeV/c^2}$ to $0.2\,\mathrm{GeV/c^2}$. The change of signal yields by this increase is

$$\Delta\text{signal yield} = 6.4, \tag{4.3}$$

which has 19 % contribution to the cross section.

These two sources have 21 % contribution to the total systematic uncertainty.

4.4 Discussions

The obtained signal yields are

$$32 \pm 43(\text{stat.}) \pm 6(\text{syst.}) \tag{4.4}$$

and the cross section upper limit at C.L. 95 % is

$$\sigma_{\text{upper limit at C.L.=95 \%}}(e^+e^- \to c\bar{c}c\bar{c}) = 24.5\,\text{pb}. \tag{4.5}$$

The Belle and BaBar measured $\sigma(e^+e^- \to J/\psi c\bar{c})$ and $\sigma[e^+e^- \to J/\psi\eta_c(\gamma)]\times\mathcal{B}_{>2}$ to be

$$\sigma(e^+e^- \to J/\psi c\bar{c}) = 0.74 \pm 0.08^{+0.09}_{-0.08}\,\text{pb (Belle) [29]}, \tag{4.6}$$

$$\sigma[e^+e^- \to J/\psi\eta_c(\gamma)] \times \mathcal{B}_{>2} = 25.6 \pm 2.8 \pm 3.4\,\text{fb (Belle) [8]}, \tag{4.7}$$

$$\sigma[e^+e^- \to J/\psi\eta_c(\gamma)] \times \mathcal{B}_{>2} = 17.6 \pm 2.8^{+1.5}_{-2.1}\,\text{fb (BaBar) [9]}. \tag{4.8}$$

Comparing the measurements we can see that $P(c\bar{c} \to \eta_c)$, the probability that $c\bar{c}$ is hadronized to η_c, is in the range between 1/20 and 1/30. If we assign 1/20 to $P(c\bar{c} \to J/\psi)$ then we have

$$\sigma(e^+e^- \to c\bar{c}c\bar{c}) \approx 15\,\text{pb}. \tag{4.9}$$

The cross section sensitivity, $\sigma_{\text{upper limit at CL=95 \%}}(e^+e^- \to c\bar{c}c\bar{c}) = 25.4\,\text{pb}$, measured in this study is in the same order as the rough estimation , $\sigma(e^+e^- \to c\bar{c}c\bar{c}) \approx 15\,\text{pb}$, based on the Belle and BaBar measurements [29], [8], [9].

Chapter 5

Conclusions

We set the cross section upper limit of $e^+e^- \to c\bar{c}c\bar{c}$ at 95 % confidence level to

$$\sigma_{\text{upper limit at CL = 95 \%}}(e^+e^- \to c\bar{c}c\bar{c}) = 24.5\,\text{pb} \tag{5.1}$$

which is compatible with a simple estimation from recent Belle and BaBar measurements [29], [8], [9]. However, the significance of this study is 0.7σ. Thus we may need more D^0 decay modes to improve the result statistically.

Appendix A

KSFW

The modified Super Fox Wolfram moment, which is also called Kakuno's Super Fox Wolfram (KSFW) moment needs 17 input variables. In Figure A.1 the distributions of the 17 input variables are shown. The solid distribution is from signal MC and the dashed one is from sideband of real data. The variable R_2 which is generally used for continuum suppression is defined to be H_2/H_0 where H_2 and H_0 are the second and the zeroth Fox Wolfram moment [25], respectively. Its correspondence to KSFW is Roo0, Rso02, Rso12, and Rso24. KSFW enhances the distinction by constructing Fisher discriminant which linearly combines all 17 variables.

The KSFW has large dependence on mm^2 [30]. Thus it is separated into 7 mm^2 regions. Table A.1 shows the seven mm^2 regions.

Table A.1: 7 mm^2 regions.

region	imm0	imm1	imm2	imm3	imm4	imm5	imm6
mm^2	$\sim$	-0.5	0.3	1.0	2.0	3.5	6.0
	-0.5	$\sim$0.3	$\sim$1.0	$\sim$2.0	$\sim$3.5	$\sim$6.0	$\sim$

The Figure A.2 shows the KSFW distributions in 7 mm^2 regions. a) shows the relative number of entries in each mm^2 region and b) - h) indicate the KSFW distributions in each mm^2 region.

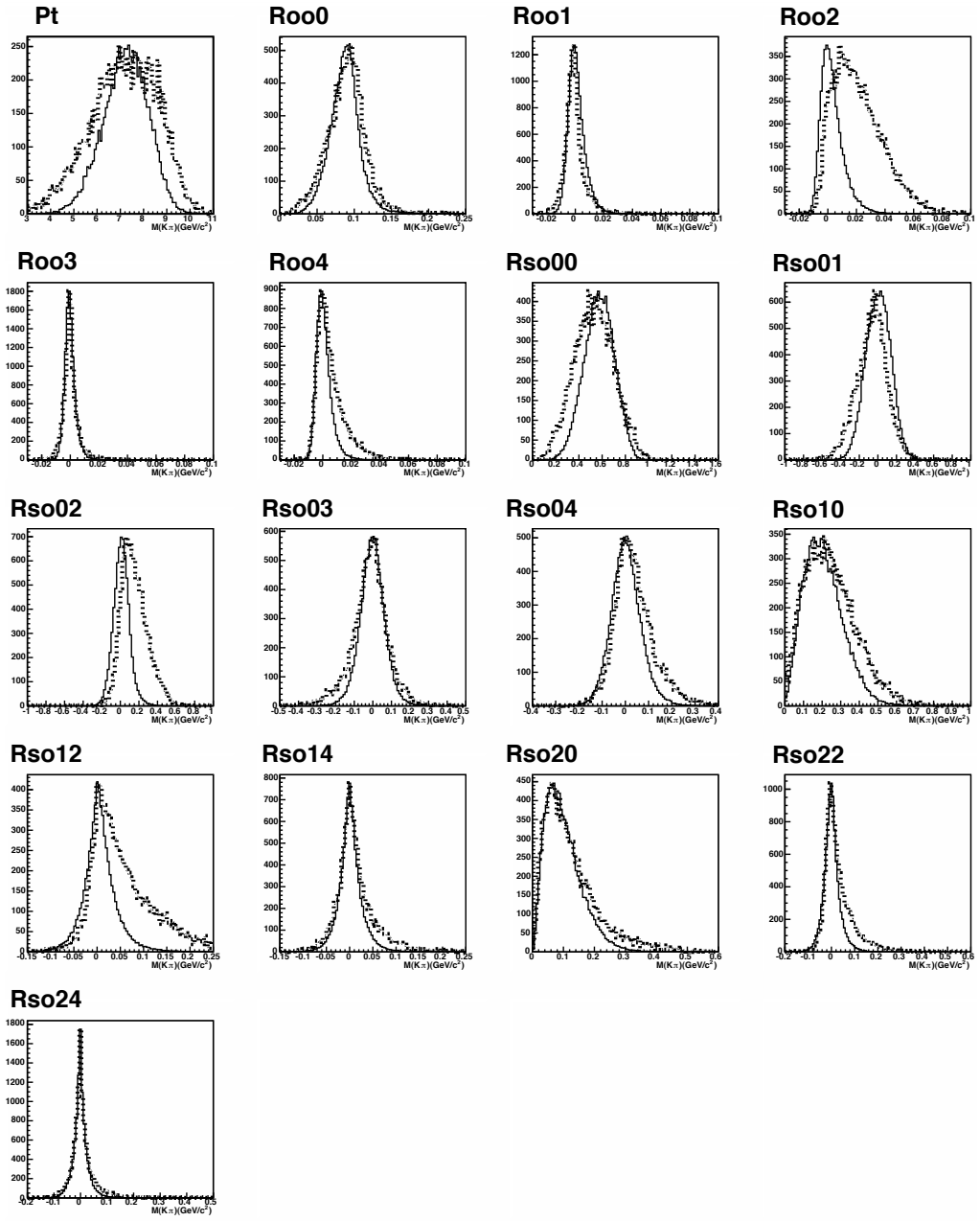

Figure A.1: The 17 input variables of KSFW for signal MC (solid) and sideband of real data (dashed).

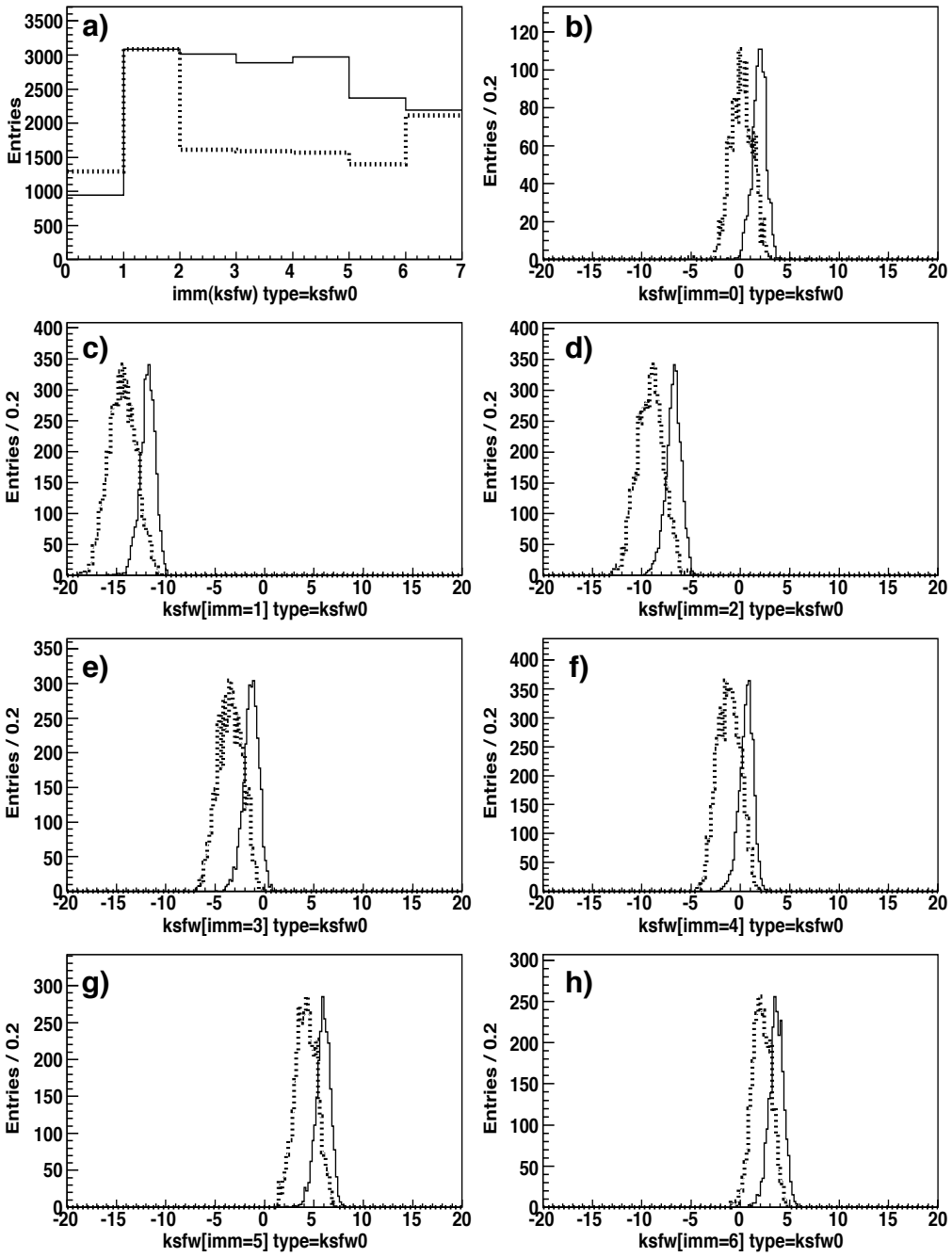

Figure A.2: a) relative number of entries and b) - h) KSFW distributions in 7 mm^2 regions. Solid distributions are from signal MC and dashed distributions are from sideband of real data.

Appendix B

Comparison of sideband subtraction with 2D mass fit

In order to confirm the validation of the sideband subtraction method, the signal yield is extracted from the 2 dimensional mass distribution of the first and second D^0s. Signal efficiency is compared for the validation check. Signal MC is used throughout the confirmation.

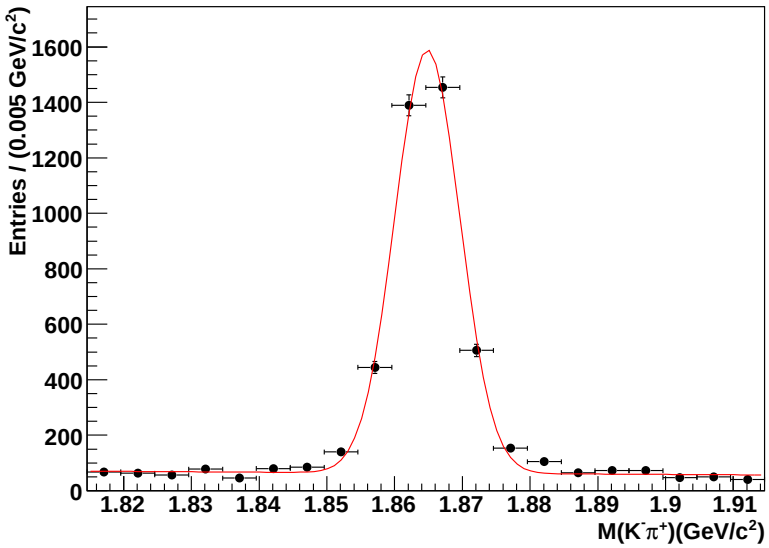

Figure B.1: Sideband subtracted mass distribution of the second D^0 and fitting result. The horizontal error bars indicate the bin size and the vertical error bars are incorporated statistically only.

Figure B.1 shows the sideband subtracted mass distribution of the second D^0.

Fitting with a fit function,

$$Gaussian + 1st\,polynomial, \tag{B.1}$$

is done to the distribution with all parameters floating. The *Gaussian* is responsible for the signal.

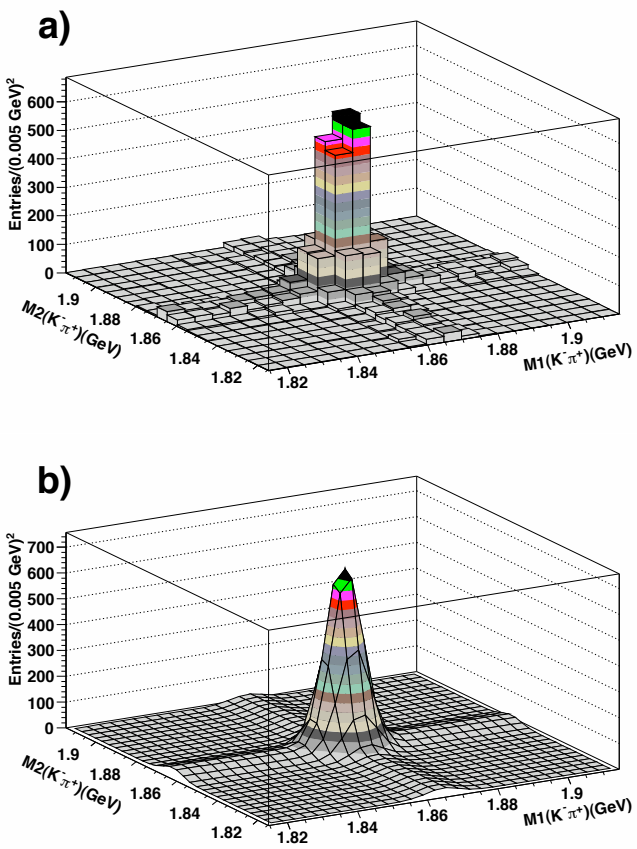

Figure B.2: a) 2 dimensional mass distribution of the first D^0 and second D^0. b) shows the corresponding fit function. M1 and M2 are the invariant masses of the first and the second D^0, respectively.

The two dimensional mass distribution and the corresponding fit function is shown in Figure B.2. Fitting is done to the distribution with a fit function,

$$(Gaussian + 1st\,polynomial) \times (Gaussian + 1st\,polynomial), \tag{B.2}$$

and the *Gaussian* × *Gaussian* is responsible for the signal. Signal MC is used and klr > 0.85. All parameters are floating.

Table B.1: The number of signal events and signal efficiencies obtained by two methods, sideband subtraction and 2 dimensional mass fit. Events are counted out of $30,000$ generated signal events.

	Sideband subtraction	2D mass fit
Number of signal events	3670 ± 110	3650 ± 720
signal efficiency ϵ_{sig}	0.122 ± 0.004	0.122 ± 0.024

As shown on the Table B.1, the signal efficiencies obtained by the two methods are consistent. We can conclude that the sideband subtraction extracts correct signal yields.

Appendix C

Error estimation of a function of independent variables

For a function of two variables, the error is calculated from

$$\delta f = \left[\left(\frac{\partial f}{\partial x_1}\delta x_1 + \frac{\partial f}{\partial x_2}\delta x_2\right)^2\right]^{\frac{1}{2}} \tag{C.1}$$

$$= \left[\begin{array}{l} \left(\frac{\partial f}{\partial x_1}\right)^2 (\delta x_1)^2 + \left(\frac{\partial f}{\partial x_2}\right)^2 (\delta x_2)^2 \\ \qquad +2\left(\frac{\partial f}{\partial x_1}\right)\left(\frac{\partial f}{\partial x_2}\right)(\delta x_1)(\delta x_2) \end{array}\right]^{\frac{1}{2}}. \tag{C.2}$$

The last term vanishes if x_1 and x_2 are independent. Then the error becomes

$$\delta f = \left[\left(\frac{\partial f}{\partial x_1}\right)^2 (\delta x_1)^2 + \left(\frac{\partial f}{\partial x_2}\right)^2 (\delta x_2)^2\right]^{\frac{1}{2}}. \tag{C.3}$$

If we generalize it for a function of n independent variables, the error becomes

$$\delta f = \left[\left(\frac{\partial f}{\partial x_1}\right)^2 (\delta x_1)^2 + \left(\frac{\partial f}{\partial x_2}\right)^2 (\delta x_2)^2 + \ ... \ + \left(\frac{\partial f}{\partial x_n}\right)^2 (\delta x_n)^2\right]^{\frac{1}{2}}. \tag{C.4}$$

For the calculation of signal yields in chapter 3, we need to calculate the error of $f(x_1, x_2) = Ax_1x_2$ where A is a constant. In this case the overall error becomes

$$\delta f = \left[\left(\frac{\partial f}{\partial x_1}\right)^2 (\delta x_1)^2 + \left(\frac{\partial f}{\partial x_2}\right)^2 (\delta x_2)^2\right]^{\frac{1}{2}} \tag{C.5}$$

$$= \left[(Ax_2)^2 (\delta x_1)^2 + (Ax_1)^2 (\delta x_2)^2\right]^{\frac{1}{2}} \tag{C.6}$$

$$= |A| \left[x_2^2 (\delta x_1)^2 + x_1^2 (\delta x_2)^2\right]^{\frac{1}{2}}. \tag{C.7}$$

When there are four variables,in other words, $f(x_1, x_2, x_3, x_4) = Ax_1x_2x_3x_4$, the error is calculated by

$$\delta f = \left[\sum_{i=1}^{4} \left(\frac{\partial f}{\partial x_i}\right)^2 (\delta x_i)^2\right]^{\frac{1}{2}} \tag{C.8}$$

$$= |A| \left[\begin{array}{r} (\delta x_1)^2 x_2^2 x_3^2 x_4^2 + x_1^2 (\delta x_2)^2 x_3^2 x_4^2 \\ +x_1^2 x_2^2 (\delta x_3)^2 x_4^2 + x_1^2 x_2^2 x_3^2 (\delta x_4) \end{array}\right]^{\frac{1}{2}}. \tag{C.9}$$

As an example, we can calculate the error of signal efficiency using eq. (C.5). The signal efficiency is defined by

$$\epsilon_{\text{sig}} = \frac{N_m}{N_g} \tag{C.10}$$

where N_m and N_g are the number of measured and generated events, respectively. Since N_m and N_g follow poison distribution, $\delta N_m = \sqrt{N_m}$ and $\delta N_g = \sqrt{N_g}$. Thus, the error of ϵ_{sig} becomes

$$\delta\epsilon_{\text{sig}} = \left[\left(\frac{\partial \epsilon_{\text{sig}}}{\partial N_m}\right)^2 (\delta N_m)^2 + \left(\frac{\partial \epsilon_{\text{sig}}}{\partial N_g}\right)^2 (\delta N_g)^2\right]^{\frac{1}{2}} \tag{C.11}$$

$$= \left[\left(\frac{1}{N_g}\right)^2 N_m + \left(-\frac{N_m}{N_g^2}\right)^2 N_g\right]^{\frac{1}{2}} \tag{C.12}$$

$$= \left[\frac{N_m}{N_g^2} + \frac{N_m^2}{N_g^3}\right]^{\frac{1}{2}} \tag{C.13}$$

$$= \frac{N_m}{N_g}\left[\frac{1}{N_m} + \frac{1}{N_g}\right]^{\frac{1}{2}}. \tag{C.14}$$

Bibliography

[1] PYTHIA; http://home.thep.lu.se/ torbjorn/Pythia.html.

[2] B. Andersson, G. Gustafson, G. Ingelman and T. Sjostrand, Phys. Rept. **97**, 31 (1983).

[3] Belle Collaboration, K. Abe *et al.*, Phys. Rev. Lett. **89**, 142001 (2002).

[4] E. Braaten and J. Lee, Phys. Rev. D **67**, 054007 (2003).

[5] K. Y. Liu, Z. G. He and K. T. Chao, Phys. Lett. B **557**, 45 (2003) [arXiv:hep-ph/0211181].

[6] D. Kang, J. W. Lee, J. Lee, T. Kim and P. Ko, Phys. Rev. D **71**, 071501 (2005).

[7] G. T. Bodwin, J. Lee and C. Yu, Phys. Rev. D **77**, 094018 (2008).

[8] K. Abe *et al.* Belle Collaboration, Phys. Rev. D **70**, 071102 (2004).

[9] B. Aubert *et al.* [BABAR Collaboration], Phys. Rev. D **72**, 031101 (2005) [arXiv:hep-ex/0506062].

[10] KEKB B Factory Design Report, KEK Report 95-7(1995) unpublished; Y. Funakoshi *et al.*, Proc. 2000 European Particle Accelerator Conference, Vienna (2000)

[11] A. Abashian *et al.* [BELLE Collaboration], Nucl. Instrum. Meth. A **479**, 117 (2002).

[12] G. Alimonti *et al.* [BELLE Collaboration], Nucl. Instrum. Meth. A **453**, 71 (2000).

[13] Belle SVD Upgrade Technical Design Report(2001), Belle SVD Group.

[14] S. Uno, Nucl. Instrum. and Meth. A **379**, 421 (1996); H. Hirano *et al.*, KEK Preprint 2000-2; M. Akatsu *et al.*, DPNU-00-06.

[15] T. Iijima *et al.*, "Aerogel Cherenkov counter for the Belle detector", Proceedings of the 7th International Conference on Instrumentation for Colliding Beam Physics, Hamamatsu, Japan, Nov. 15-19, 1999.

[16] H. Kichimi *et al.*, "The Belle TOF system", Proceedings of the 7th International Conference on Instrumentation for Colliding Beam Physics, Hamamatsu, Japan, Nov. 15-19, 1999.

[17] A Study of CP Violation in B Meson Decays, Technical Design Report, KEK Report 95-1 (1995).

[18] H. Ikeda *et al.*, Nucl. Instrum. Meth. A **441**, 401 (2000).

[19] A. Pukhov, E. Boos, M. Dubinin, V. edneral, V. Ilyin, E. Kovalenko, A. Kryukov, V. Savrin, S. shichnin and A. Semenov, hep-hp/9908288 (1999).

[20] EvtGen; http://www.slac.stanford.edu/∼lange/EvtGen/.

[21] Geant; http://geant4.cern.ch/.

[22] GSIM; http://belle.kek.jp/ harat/Gsim/gsim.html.

[23] E. Won, H. C. Ha, J. H. Choi, and D. Kang, J. Korean Phys. Soc. **48**, 202 (2006).

[24] H. Kakuno *et al.*, Nucl. Instrum. Meth. A **533**, 516 (2004).

[25] G. C. Fox and S. Wolfram, Phys. Rev. Lett. **41**, 1581 (1978).

[26] R. A. Fisher, Annals of Eugenics **7**, 179 (1936).

[27] D. Kang, T. Kim, J. Lee and C. Yu, Phys. Rev. D **76**, 114018 (2007)

[28] Eunil Won, Ph.D. Thesis, University of Rochester (1996).

[29] P. Pakhlov, Belle Internal Note #1071.

[30] Yuuji Unno, Ph.D. Thesis, Chiba University (2004).